The KLOE drift chamber

The KLOE Collaboration [1]

presented by A. Ferrari

Università di Roma Tre e INFN - Via della Vasca Navale, 84 - I-00146 Roma

Abstract

The design and construction of the large drift chamber of the KLOE experiment is presented. The track reconstruction is described, together with the calibration method and the monitoring systems. The stability of operation and the performance are studied with samples of e^+e^-, $K_S K_L$ and K^+K^- events.

1 Introduction

The KLOE experiment [1] at the Frascati ϕ-factory DAΦNE has been designed with the main goal of precisely measuring the CP-symmetry violation parameters in the decay of neutral kaons. The double-ring e^+e^- collider DAΦNE [2] operates at a center of mass energy of $\sim$ 1020 MeV, the mass of the ϕ meson. Equal-energy electrons and positrons collide at an angle of 26 mrad. ϕ mesons are produced with a cross section of $\sim 3\ \mu$b, and are nearly at rest, with a small transverse momentum of $\sim$ 13 MeV/c. Neutral kaons are coherently produced through the decay $\phi \to K^0 \bar{K}^0$. The kaon pairs are in an antisymmetric state, giving rise to the weak eigenstates $K_L K_S$.
The design of the KLOE drift chamber [3, 4] was driven by the event topology

[1] A. Aloisio, F. Ambrosino, A. Antonelli, M. Antonelli, C. Bacci, R. Baldini-Ferroli, G. Bencivenni, S. Bertolucci, C. Bini, C. Bloise, V. Bocci, F. Bossi, P. Branchini, S. A. Bulychjov, G. Cabibbo, R. Caloi, P. Campana, G. Capon, G. Carboni, M. Casarsa, V. Casavola, G. Cataldi, F. Ceradini, F. Cervelli, F. Cevenini, G. Chiefari, P. Ciambrone, S. Conetti, E. De Lucia, G. De Robertis, P. De Simone, G. De Zorzi, S. Dell'Agnello, A. Denig, A. Di Domenico, C. Di Donato, S. Di Falco, A. Doria, M. Dreucci, O. Erriquez, A. Farilla, G. Felici, A. Ferrari, M. L. Ferrer, G. Finocchiaro, C. Forti, A. Franceschi, P. Franzini, C. Gatti, P. Gauzzi, A. Giannasi, S. Giovannella, E. Gorini, F. Grancagnolo, E. Graziani, S. W. Han, M. Incagli, L. Ingrosso, W. Kluge, C. Kuo, V. Kulikov, F. Lacava, G. Lanfranchi, J. Lee-Franzini, D. Leone, F. Lu, M. Martemianov, M. Matsyuk, W. Mei, L. Merola, R. Messi, S. Miscetti, M. Moulson, S. Mueller, F. Murtas, M. Napolitano, A. Nedosekin, F. Nguyen, M. Palutan, L. Paoluzi, E. Pasqualucci, L. Passalacqua, A. Passeri, V. Patera, E. Petrolo, G. Pirozzi, L. Pontecorvo, M. Primavera, F. Ruggieri, P. Santangelo, E. Santovetti, G. Saracino, R. D. Schamberger, B. Sciascia, A. Sciubba, F. Scuri, I. Sfiligoi, T. Spadaro, E. Spiriti, G. L. Tong, L. Tortora, E. Valente, P. Valente, B. Valeriani, G. Venanzoni, S. Veneziano, A. Ventura, G. Xu, G. W. Yu.

Preprint submitted to Elsevier Science *13 May 2002*

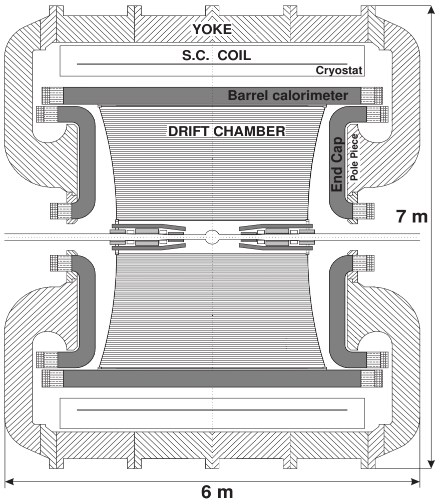

Fig. 1. *Cross section of the KLOE detector, along the beam line.*

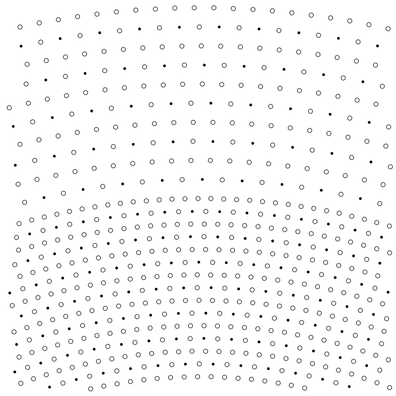

Fig. 2. *Drift cell configuration in a portion of the plane z=0. The field:sense ratio (open circles and full dots in the figure) is 3:1.*

of the K_L decays: K_L's have a mean free path of 343 cm, and vertices that are mostly distributed at large polar angles (proportionally to $\sin^2\theta$, with respect to the beam axis). To maximize the acceptance for the decays into charged and neutral channels, a large tracking volume is therefore required, together with a high and uniform reconstruction efficiency and a good momentum resolution ($\sigma_{p_T}/p_T \simeq 0.4\%$). Additional requirements are high transparency, to reduce regeneration, multiple scattering and conversion of low energy photons, and good self-calibrating capabilities.

2 Construction solutions

The geometrical solution has been a uniform cell structure on a large cylindrical volume, 3.3 m in length and 2 m in radius, around the interaction point (see Fig. 1). The drift chamber is surrounded by a lead-scintillating fiber sampling calorimeter [5], and both are immersed in a magnetic field of 0.52 T provided by a superconducting coil.

The uniform filling of the chamber has been achieved through a structure of drift cells "almost" square-shaped, arranged in coaxial layers with alternating stereo angles which increase in magnitude with radius from ± 60 mrad to ± 150 mrad. The ratio of field to sense wires (3:1) is a satisfactory compromise in maximizing the track sampling frequency, while maintaining as well as possible the electrostatic stability of the drift cell [6, 7]. Fig. 2 shows a portion of the layout of the wires at the boundary between the 12 inner and the 46 outer layers: the corresponding cell areas are 2×2 cm^2 and 3×3 cm^2 respectively, for a total of 12582 single-sense-wire cells and 52140 wires. Materials were chosen in order to minimize the matter density along the path of neutral kaons, charged particles and photons. A carbon fiber composite ($\leq$ 0.1 X_0) has been chosen for the chamber shell. The gas used is a 90% helium, 10% isobutane mixture. Its relevant properties, either measured directly [8, 9, 10], or computed with transport equations [11, 12], are listed in Tab. 1.

Gas parameter	**Value**		**Ref.**
N. primary clusters	12.3 ± 0.2 cm^{-1}		[8, 9]
Total specific ionization	~ 9 cm^{-1}		[9]
Drift velocity	17–23 mm/μs	E= 0.5-1 kV/cm	[8]
Drift angle	0.2–0.3 rad	E= 0.5-1 kV/cm	[8, 11]
Diffusion coefficient	$(3.2–2.5)\times10^{-4}$cm^2/μs	E= 0.5-1 kV/cm	[10]
Radiation length	~ 1300 m		

Table 1
Properties of the 90% He - 10% iC_4H_{10} gas mixture. The first two parameters are given for a minimum ionizing particle.

The choice of helium has posed certain challenges. The non-saturated drift velocity requires tight control of the gas mixture, as well as of the whole calibration procedure. Moreover, helium leaks more rapidly then any other gas. A reliable gas system [4, 13] guarantees operation limits of $\pm$ 0.1% in isobutane concentration and $\pm$ 0.1 mbar in differential pressure.
Gold-plated tungsten wires (diam. = 25 μm) are used as anodes. For the field wires, silver-plated aluminum wires (diam. = 80 μm) have been chosen. The average value of the radiation length in the whole chamber volume is $\sim$ 900 m.

3 Tracking

The track reconstruction package [14] proceeds by three steps: pattern recognition, track fit and vertex fit. The pattern recognition begins by associating hits, working inward from the outermost layers. Starting from the hit association in the transverse plane, track candidates for the two separate stereo views are built and merged together. The track fit is obtained from the standard minimization procedure of the function $\chi^2 = \sum_1^{N_{\rm hits}} [d_n - d_n^{\rm fit}]/\sigma_n^2$, where $d_n(t_{\rm drift})$ are the drift distances obtained via space-time (s-t) relation from the measured drift times, $d_n^{\rm fit}$ are the results of the fit and σ_n^2 are estimates of the hit resolutions. The procedure is iterative because the s-t relations depend on the track parameters. At each tracking step, the effects due to energy loss and multiple scattering are estimated. Dedicated algorithms are also used to add hits missed by the pattern-recognition algorithm, to reject wrongly associated hits, to identify kinks, and to join split tracks.

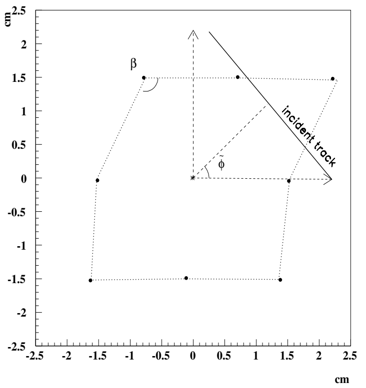

Fig. 3. *The β and $\tilde{\phi}$ angles.*

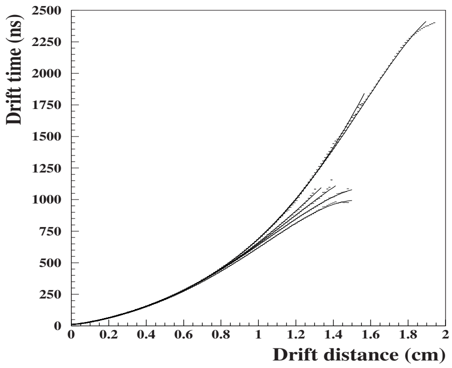

Fig. 4. *s-t relations for different incidence angles $\tilde{\phi}$, for 3×3 cells with the same shape.*

4 Parametrization and calibration of s-t relations

The peculiar geometry, together with the non-saturated gas mixture, complicates the description of s-t relations.
Let us consider an ionization cluster released by a charged track coming from a K_L decay. Depending on the drift direction (which is identified by the $\tilde{\phi}$ angle in Fig. 3), this cluster "moves" with a different s-t relation, because the shape of the electric field changes with $\tilde{\phi}$. Moreover, because of the full stereo geometry, the distortion of the cell (described by the β angle) is a function of all the spatial coordinates. A satisfactory parametrization of the s-t relations [15, 18] has been obtained by considering 6 reference cells in β and 36 bins in the crossing angle for each cell type (large or small): in total, 232 s-t relations.
Because of the non-linearity, 5^{th} order polynomials are used. Since the linear and parabolic terms must not change too much with respect to the higher order terms (reflecting in a realistic way the changing of s-t relations with the ambient parameters), the Chebyshev polynomials, which form a complete set of orthonormal polynomials, have been chosen. The measured drift time t_{drift} is then parametrized as:

$$t_{\text{drift}} = P_{\text{Cheb}}(d) = C_0 + R_1(d) + R_2(d) + R_3(d) + R_4(d) + R_5(d),$$

where d is the impact parameter between the track and the sense wire and the five polynomials $R_i(C_i, d)$ are fixed by the coefficients C_i. Calibrating the s-t relations means therefore fixing all the sets of Chebyshev coefficients. Cosmic-ray events are used, because they allow complete cell coverage in terms of β and $\tilde{\phi}$, with enough statistics. The first step of the calibration procedure [18] is the reconstruction of the cosmic-event sample. Since the trajectory of the particle is unknown at the level of the pattern-recognition procedure, there is no information about the value of the $\tilde{\phi}$ and β parameters. The cell response is therefore described at this level by only two s-t relations (one for each cell type), which are an average over all of the track orientations and drift cell shapes. Using this "raw" description (parametrized using a combination of three polynomials), the pattern-recognition algorithm finds the track candidates for each event, allowing $\tilde{\phi}$ and β angles to be estimated. Then, the track fit procedure computes the impact parameters d_n for each hit associated to a track candidate by inverting the appropriate Chebyshev polynomial. The 6×232 C_i^k coefficients ($k=1,\ldots,232$) define the "fine" s-t relations which account for the cell type, the track orientation and the cell deformation parameter. The input values of the C_i^k coefficients, as well as the values of the "raw" parameters and the resolution functions $\sigma(d)$, are set equal to the values calculated in the previous calibration run. The residuals related to the "fine" and "raw" s-t relations ($r_n^{\text{fine}}=d_n^{\text{fit}}-d_n(C_i^k,t_{\text{drift}})$; a similar definition holds for the "raw" relations) are binned in 300 μm-wide intervals [2] of drift distance fitted with Gaussians. The values of the fit are then used to correct s-t relations in a subsequent iteration. The procedure is halted when for each of the 232 histograms the average (over the 300 μm-wide bins) of the residual distribution is smaller than 40 μm. This condition, which has to be satisfied at the first iteration in order to classify a sample as "calibrated," has been chosen after a Monte Carlo study of track and vertex reconstruction efficiencies versus different levels of simulated miscalibration. $K_L\to\pi^+\pi^-$ and $K_S\to\pi^+\pi^-$ events have been used. The different levels of miscalibration have been simulated by moving the average values $\langle r\rangle$ of the residual distribution. Some results are shown in Tab. 2. The $K_L\to\pi^+\pi^-$ total reconstruction efficiency decreases by almost 1.7% passing from $\langle r\rangle\sim 10\,\mu$m to $\langle r\rangle\sim 50\,\mu$m. This is mostly due to the contribution from the K_L time of flight, which heavily affects the hit residuals of K_L tracks [3]. The reconstruction efficiency for the K_S decay is much less sensitive, varying only by -0.3% under the same changes in the residual levels. Tab. 2 also shows, for the K_L sample, a study of the vertex spatial resolution as a function of the calibration accuracy. This dependence is significant for K_L vertices, which are completely reconstructed within the tracking volume, while it is negligible for K_S vertices, which are more affected by the uncertainty in the extrapolation of $\pi^\pm$ tracks through the drift chamber inner wall.

At the end of the iterative procedure, a new reconstruction of the sample is performed in order to fit the new s-t relations. Each histogram of t_{drift} versus d_n^{fit} is sliced in 110 μm-wide bins of d_n, a Gaussian fit is performed in each slice and the estimated mean values are used to plot and finally fit the s-t curve

[2] The bin width has been chosen to be on the order of the expected spatial resolution: $\simeq 200\,\mu$m.

[3] a residual level $\langle r\rangle\sim 10\,\mu$m measured on the K_S tracks - or equivalently on the cosmic-ray tracks during the calibration - corresponds to $\langle r\rangle\sim 77\,\mu$m on the K_L tracks.

	$K_S \to \pi^+\pi^-$	$K_L \to \pi^+\pi^-$			
$\langle r \rangle$ [μm]	$\varepsilon_{\rm tot}$ [%]	$\varepsilon_{\rm tot}$ [%]	$\sigma_{\rm vtx}(\hat{x})$ [μm]	$\sigma_{\rm vtx}(\hat{y})$ [μm]	$\sigma_{\rm vtx}(\hat{z})$ [mm]
10	92.50	77.50	400	400	1.3
30	92.43	76.61	470	450	1.35
50	92.15	76.15	500	450	1.45
70	92.19	75.68	550	500	1.5

Table 2
Monte Carlo reconstruction efficiencies and vertex resolutions for $K_{L,S} \to \pi^+\pi^-$ decays, as a function of the miscalibration in the central part of each cell.

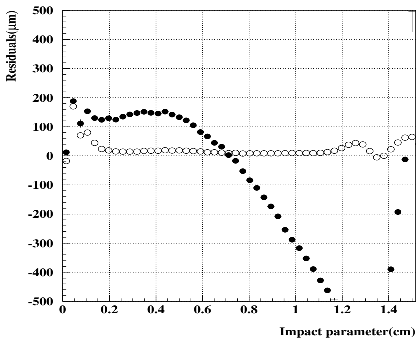

Fig. 5. *Mean values of the residual distributions at the beginning and at the end of the calibration procedure, (3×3 cells, $\tilde{\phi}$ ∼0).*

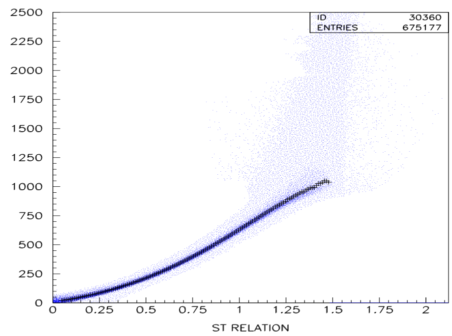

Fig. 6. $t_{\rm drift}$ *vs* d_n *at the end of the iterative procedure (hits in 3×3 cells, $\tilde{\phi}$ ∼0). The fit of the new s-t relation is superimposed.*

(see Fig. 6). The new constants are written into the database.

4.1 Spatial resolution

The resolution has been evaluated in each bin of reconstructed impact parameters as the standard deviation of the Gaussian fit to the distribution of the residuals [18]. Fig. 7 shows the resolution averaged over all the "fine" parametrizations, as a function of the reconstructed impact parameter. The spatial resolution is better than 200 μm over a large part of the cell, independently of the azimuthal direction of the tracks and the cell shape. The resolution curve can be fitted with the quadratic sum of the three contributions from the primary ionization statistics, the longitudinal electron diffusion, and the uncertainty in the drift time measurement due to electronic noise. Fig. 8 shows these fitted contributions. The best fit for the primary ionization statistics, parametrized as a function of the mean free path λ between two consecutive ionizing collisions, gives λ=(770 ± 14) μm, corresponding to

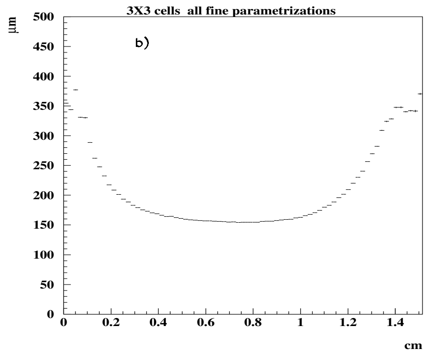

Fig. 7. *Resolution as a function of the impact parameter (3×3 cells).*

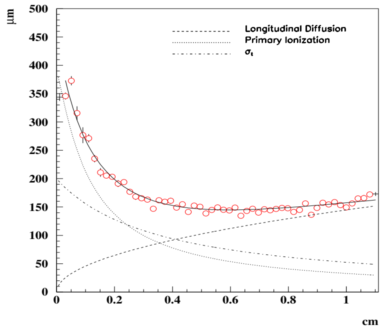

Fig. 8. *Different contribution to the spatial resolution.*

(12.9 ± 0.1) clusters per cm for a minimum ionizing particle. The longitudinal diffusion contribution has been estimated to be $\sigma_D \simeq$140 μm for 1 cm of drift. These values are in good agreement with the results in Tab. 1. The contribution due to the time resolution, which in Fig. 8 is multiplied by the local drift velocity, is constant in the time domain and has been estimated to be σ_t=(4.8 ± 0.2) ns.

5 Monitoring the drift chamber performance

The calibration program described in the previous sections works in a more general online architecture. A synchronous procedure automatically starts at the beginning of each run and reconstructs selected cosmic-ray events. Events with two reconstructed calorimeter clusters are filtered, requiring a time of flight consistent with a single particle crossing the detector. The time of each cell is corrected assuming a straight line joining the two calorimeter clusters. These events pass through the described calibration procedure, which with 80 000 acquired events performs the check of the residuals in the central part of the cell. If the value exceeds the 40 μm level, 300 000 cosmic-ray events are collected and used to calibrate the s-t relations. Based on our experience during the data taking periods, all of the gas parameters are very stable, except for the atmospheric pressure which can change several times in a month. The online calibration procedure is able to follow any changes, rapidly correcting miscalibration at the level of 100 μm at the cell border (corresponding to variations of the pressure of $\sim$ 20 mbar) before the offline event recostruction.
Due to the background rate generated by DAΦNE, the integrated charge on the wires could in principle give some ageing problems. By looking at the run averaged current drawn by a HV channel, the measurement of the integrated charge [19] comes by straightforward integrating over the operation time, and dividing by the number of wires served by a single channel. The integrated charge in October 2001 was $\sim$ 0.3 mC/cm, which is a safe value, according

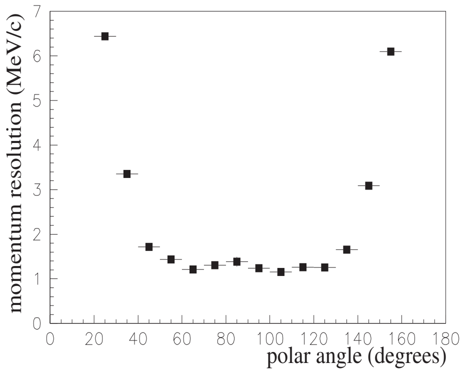

Fig. 9. *Momentum resolution for 510 MeV electron and positron tracks from Bhabha scattering, as a function of the polar angle of emission.*

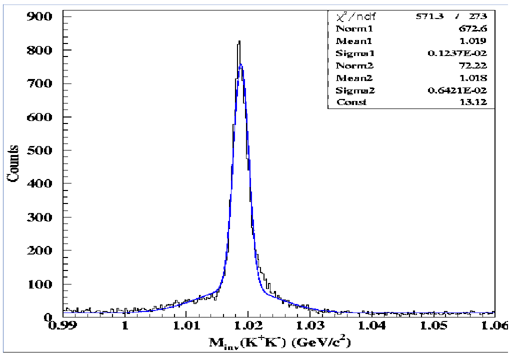

Fig. 10. *The invariant mass of the ϕ, reconstructed with charged kaon decays.*

to the test performed on a KLOE cell prototype [20], and to existing measurements with different hydrocarbon gas mixtures [21]. In order to study the machine background, a method to monitor the wire counting rate due to the noise in the inner layers of the chamber has been developed. The measurement is performed by analyzing the drift time spectra integrated on each single layer, looking at the number of hits in a time window out of the signal region. The procedure allows the noise rate to be estimated every $\sim$ 90 sec.

6 Monitoring the physical quantities

Samples of Bhabha-scattering events allow evaluation of the momentum resolution for 510 MeV $e^{\pm}$, as well as the beam energy at the interaction point and the position and the shape of the luminous region. Fig. 9 shows the momentum resolution for these e^+e^- tracks: in the interval $50° < \theta <130°$, where the projected track length on the transverse plane is constant, $\sigma_p \simeq 1.3$ MeV and $\sigma_p/p = 2.5\times10^{-3}$.
The position and the shape of the interaction region are measured online by finding the point of closest approach of the tracks to the z axis, and using the transverse momentum of the two tracks [22]. With a typical sample of 10^4 events, the position is measured with an accuracy of $\sim$ 60 μm in the x,y plane and $\sim$ 1 mm in z. The shape is measured with an experimental resolution of 0.5 mm in the x,y plane and $\sim$ 1 mm in z.
In measuring $\sqrt{s}$, a statistical accuracy at the level of $\sim$ 5 KeV is obtained with the sample of Bhabha-scattering events that are selected online during a typical run of 100 nb^{-1}.
Fig. 10 shows the invariant mass of the ϕ, reconstructed by using a sample of $\phi \to K^+K^-$ events: after the heavy correction for $K^{\pm}$ energy loss, the Gaus-

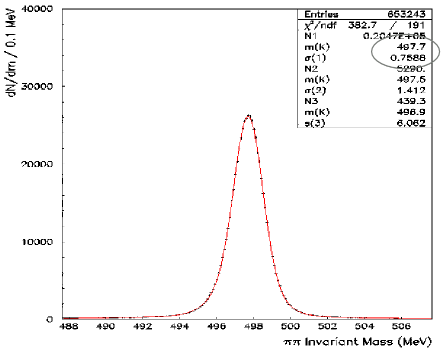

Fig. 11. *The K_S reconstructed invariant mass.*

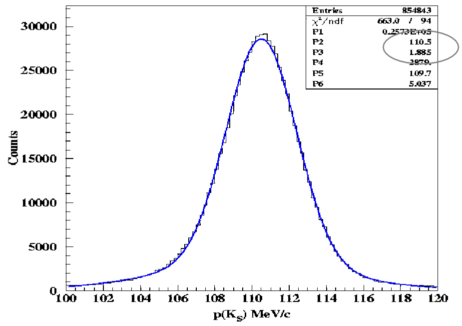

Fig. 12. *The K_S reconstructed momentum.*

sian fit to the central peak gives σ ~1.2 MeV.
$K_S \to \pi^+\pi^-$ decays are clearly identified, the signature being the right value of the reconstructed invariant mass with two unlike sign tracks, that are coming from a vertex within 6 cm from the center of the luminous region (Fig. 11). Fig. 12 shows the reconstructed K_S momentum, where the resolution of $\sim$ 1.8 MeV is consistent with the results obtained for the single-track analysis.

7 Conclusions

The KLOE drift chamber has been built with very demanding specifications. About 3 years of operation show that the detector works efficiently and in a stable way. The calibration is fully reliable and the tracking performance is at the per-mil level in absolute momentum calibration. The detector completely fulfils the design requirements.

Work partially supported by the German Federal Ministry of Education and Research (BMBF) contract 06-KA-957; by Graduiertenkolleg 'H.E. Phys.and Part. Astrophys.' of Deutsche Forschungsgemeinschaft, Contract No. GK 742; by INTAS, contracts 96-624, 99-37; and by TARI, contract HPRI-CT-1999-00088.

References

[1] The KLOE Collaboration, *The KLOE Detector Technical Proposal*, LNF-93/002, (1993).
S. Bertolucci for the KLOE Collaboration, *A status report of KLOE at DAΦNE*,

in Proc. of the 19th International Symposium on Lepton and Photon Interactions at High Energies, Stanford, CA U.S.A. (1999), hep-ex/0002030.

[2] The DAΦNE Project Team, *Proposal for a ϕ-factory*, LNF-90/031 1990.
S. Guiducci, *Status of DAΦNE*, in Proc. of the 2001 Particle Accelerator Conference, Chicago, IL U.S.A. (2001).

[3] The KLOE Collaboration, *The KLOE central drift chamber. Addendum to the KLOE technical proposal*, LNF-94-028 (June 1994).

[4] The KLOE Collaboration, *The Tracking Detector of the KLOE experiment*, preprint LNF-01/016(P), accepted on NIM A.

[5] G. Lanfranchi on behalf of the KLOE Collaboration, *The KLOE electromagnetic calorimeter*, this Conference.

[6] *GARFIELD, a drift chamber simulation program*, CERN program library, entry W5050.

[7] G. Finocchiaro *et al.*, Nucl. Instr. Meth. **A360**, 48 (1995).

[8] C. Avanzini at al., Nucl. Instr. Meth. **A 449**, 237 (2000).

[9] G.Bencivenni *et al.*, *The prototype 0 of the KLOE tracking chamber*, KLOE note **79** (1993).

[10] V. Golovatyuk, F. Grancagnolo, M. Primavera, Nucl. Instr. Meth. **A 394**, 97 (1997).

[11] A. Sharma and F. Sauli, Nucl. Instr. Meth. **A 350**, 470 (1994).

[12] S.F.Biagi, Nucl. Instr. Meth. **A283**, 716 (1989).

[13] U. von Hagel, A. Denig, W. Kluge, F.Schoenleber, Nucl. Instr. Meth. **A 420**, 429 (1998).

[14] A. Antonelli *et al.*, *A short description of the track reconstruction program with the KLOE drift chamber*, KLOE note **157** (1996).

[15] P. de Simone, KLOE note **98** (1994).

[16] The KLOE Collaboration, *NOVEL DAQ and Trigger Methods for the KLOE experiment*, hep-ex/0006039 (2000).

[17] The KLOE Collaboration, M. Adinolfi, *et al.*, *The KLOE trigger system*, LNF Report LNF-02/02 (P), submitted to Nucl. Instr. Meth.

[18] G. Cabibbo, P. de Simone, A. Ferrari, E. Pasqualucci, L. Passalacqua, L. Pontecorvo and T. Spadaro, *The calibration of the space-time relations in the KLOE drift chamber*, KLOE note **175** (2001).

[19] G. Finocchiaro, L. Passalacqua, P. Valente and L. Pontecorvo, KLOE memo **238** (2000).

[20] G. Bencivenni *et al.*, *Ageing test of the KLOE drift chamber wires*, KLOE note **143** (1995).

[21] J. Vavra, *Review of wire chamber ageing*, Nucl. Instr. Meth. **A 252**, 547 (1986).

[22] S. Dell'Agnello, M. Primavera, KLOE memo **202** (2000).